

# Probing electric field tunable multiband superconductivity in alternating twisted quadralayer graphene

Le Liu<sup>1,2</sup>, Yu Hong<sup>1,2</sup>, Chengping Zhang<sup>3</sup>, Jundong Zhu<sup>1,2</sup>, Jingwei Dong<sup>1,2</sup>, Kenji Watanabe<sup>4</sup>, Takashi Taniguchi<sup>5</sup>, LuoJun Du<sup>1,2</sup>, Dongxia Shi<sup>1,2,6</sup>, Kam Tuen Law<sup>3</sup>, Wei Yang<sup>1,2,6\*</sup>, Guangyu Zhang<sup>1,2,6\*</sup>

<sup>1</sup> *Beijing National Laboratory for Condensed Matter Physics and Institute of Physics, Chinese Academy of Sciences, Beijing 100190, China*

<sup>2</sup> *School of Physical Sciences, University of Chinese Academy of Sciences, Beijing, 100190, China*

<sup>3</sup> *Department of Physics, Hong Kong University of Science and Technology, Clear Water Bay, Hong Kong, China*

<sup>4</sup> *Research Center for Electronic and Optical Materials, National Institute for Materials Science, 1-1 Namiki, Tsukuba 305-0044, Japan*

<sup>5</sup> *Research Center for Materials Nanoarchitectonics, National Institute for Materials Science, 1-1 Namiki, Tsukuba 305-0044, Japan*

<sup>6</sup> *Songshan Lake Materials Laboratory, Dongguan 523808, China*

\* Corresponding authors. Email: [wei.yang@iphy.ac.cn](mailto:wei.yang@iphy.ac.cn); [gyzhang@iphy.ac.cn](mailto:gyzhang@iphy.ac.cn)

## ABSTRACT

Alternating twisted multilayer graphene presents a compelling multiband system for exploring superconductivity. Here we investigate robust superconductivity in alternating twisted quadralayer graphene, elucidating carrier contributions from both flat and dispersive bands. The superconductivity is robust, with a strong electrical field tunability, a maximum BKT transition temperature of 1.6 K, and high critical magnetic fields beyond the Pauli limit. We disentangle the carrier density of Dirac bands and flat bands from the Landau fan diagram. Moreover, we could estimate the flatband Fermi velocity from the obtained high critical current near half-filling when superconductivity is killed at finite magnetic fields, and further quantify the superfluid stiffness from the low critical current in the superconducting regime. Our results exhibit the electric field-tunable coupling strength within the superconducting phase, revealing unconventional properties with vanishing Fermi velocity and large superfluid stiffness. These phenomena, attributed to substantial quantum metric contributions, offer new insights into the mechanisms underlying unconventional superconductivity in moiré systems.

## I. INTRODUCTION

Superconductivity is characterized by flows of condensed electron pairs with zero dissipation. To understand the superconductivity, especially the multiband superconductors with high temperature superconductivity, is of fundamental interests and great promise for modern science and technology<sup>1,2</sup>. Recently, moiré superlattices composed of twisted multiple atomic thin layers give birth to topological flat band systems<sup>3</sup>, where strong correlation effects enable the observation of superconductivity<sup>4-12</sup> along with correlated insulators<sup>13-19</sup>, ferromagnetism<sup>20-22</sup>, fractional<sup>23-25</sup> or integer<sup>26-28</sup> quantum anomalous Hall effect, etc. In twisted bilayer graphene (TBG), the flat band parts are situated in moiré AA regions at a low energy, while the dispersive band parts are distributed among moiré regions at a higher energy in the band structure<sup>29</sup>; superconductivity is observed in a specific magic angle<sup>4</sup>. A more intriguing example is the alternating twisted multilayer graphene (ATMG) systems<sup>7,8,10-12,30,31</sup>, a typical multiband system hosting dispersive and flat bands<sup>32</sup>. The number of dispersive bands is  $N - 2$ , where  $N$  is the number of graphene layers. ATMG have opened new avenues to investigate robust unconventional superconductivity, hosting a widely electric field-tunable superconducting phase diagram with an enhanced critical temperature and a large in-plane magnetic field that exceeds the Pauli limit<sup>33</sup>. The hybridization between dispersive and flat bands, tunable by electrical displacement fields, triggers significant changes in superconducting coupling strength, enabling the investigation of Bardeen-Cooper-Schrieffer (BCS) to Bose-Einstein condensate (BEC) crossover<sup>7,12</sup>. Despite intensive study, the nature of superconductivity in ATMG remains elusive, particularly regarding the individual roles of dispersive bands and flat bands in the electric-field tunable superconducting behaviors. Resolving these uncertainties would shed light on the mechanism of superconductivity in twisted moiré systems and other systems as well.

Here, we focus on the superconductivity in alternating twisted quadralayer graphene (ATQG) with a twisted angle of  $1.58^\circ$ . As a member of ATMG family, ATQG is an ideal candidate to investigate the superconductivity in multi-bands systems, containing two dispersive bands and one flat band. We elucidate carrier contributions from flat and dispersive bands by analyzing Landau fan diagrams. The non-negligible contribution of dispersive bands suggests that superconductivity arises with the multiband involvement. In addition, we could quantify the Fermi velocity of the flat bands from critical current measurements outside the superconducting region and the superfluid stiffness in the superconducting region. Furthermore, we investigate the electric field-tunable superconducting behaviors, revealing enhanced coupling strength within the BCS-BEC crossover regime. Additionally, the vanishing Fermi velocity and large superfluid stiffness, deviating from the BCS theory, suggest an unconventional superconducting mechanism, likely ascribed to the enhanced quantum metric driven by electric fields.

## II. RESULTS

### A. Robust Superconductivity in ATQG System

The ATQG sample is fabricated by using the ‘cut and stack’ method<sup>34</sup>. The four monolayer pieces, cutting from one large flake of monolayer graphene, are alternately stacked with one relative twisted angle  $\theta$  (Fig. 1a), resulting in one single moiré unit cell with the size defined by  $\theta$ . In ATQG, two Dirac-type bands, located at the corner of moiré Brillouin zone  $K_s$  and  $K_s'$ , coexist with the flat band<sup>32,35</sup>, as shown in Fig. 1b. These Dirac bands are independent from the flat band at interlayer potential energy  $U = 0$ , while they hybridize with the flat band at  $U \neq 0$  with a gap opening at CNP (Fig. 1c). Fig. 1d exhibits a typical longitudinal resistance ( $R_{xx}$ ) map as a function of the total filling factor  $\nu_{\text{tot}}$  and the displacement field  $D$  at a base temperature of  $T = 30$  mK. Here, we define  $\nu_{\text{tot}} = \nu_{\text{flat}} + \nu_{\text{Dirac}} = 4n/n_0$ , where  $\nu_{\text{flat}}$  and  $\nu_{\text{Dirac}}$  correspond to the filling factor of the flat band and Dirac bands, respectively. The full filling carrier density  $n_0$  are extracted from the full filling resistance peak at  $U \neq 0$  where hybridization eliminates the discrepancy between  $\nu_{\text{tot}}$  and  $\nu_{\text{flat}}$ . It shows  $n_0 = 5.78 \times 10^{12} / \text{cm}^2$ , corresponding to a twisted angle of  $1.58^\circ$ , where the bandwidth of flat band is  $\sim 10$  meV in continuum model calculations (Fig. 1b).

We observe robust superconductivity in a wide range of the phase diagram in Fig. 1d, indicated by the two large blue-colored regions with zero resistance almost spanning from  $\nu_{\text{tot}} \sim \pm 2$  to  $\sim \pm 4$  and within a finite  $|D| < \sim 0.5$  V/nm. As shown in Fig. 1e and 1f, the resistance in these regions quickly drops to zero when the temperature is lower than 1 K. At a fixed  $\nu_{\text{tot}} = 2.31$ , the temperature-dependent resistance exhibits a typical non-linear superconducting transition with  $T_c$  of  $\sim 1.2$  K at  $D = 0$  V/nm and of  $\sim 2$  K at  $D = 0.26$  V/nm. Notably, as shown in Fig. 1g, the temperature-dependent voltage-current ( $V$ - $I$ ) curves show a clear Berezinskii–Kosterlitz–Thouless (BKT) transition at the critical temperature of  $T_{\text{BKT}} = 1.1$  K, where  $V$  is proportional to  $I^3$ , demonstrating the 2D superconducting nature in ATQG. Furthermore, evidences of phase coherence are revealed in the magnetic field response of differential resistance  $dV/dI$ , showing a weak interference pattern and a strong suppression at critical magnetic field  $B_\perp \sim 0.1$  T (inset of Fig. 1e). All the above-mentioned observations indicate these zero resistance states in the phase diagram are robust superconducting states.

## B. Coexistence of Dispersive and Flat Bands in ATQG

Compared with twisted bilayer graphene (TBG), the involvement of dispersive bands extends the regime of superconductivity and simultaneously introduces complexity into the phase diagram<sup>7,8,10–12</sup>. Before investigating the mechanism of superconductivity in ATQG, it is crucial to disentangle the transport behaviors for the two types of bands and elucidate the respective contribution to carrier densities, which can be probed from the Landau fan diagram (Methods). Fig. 2a-c show Landau fan diagrams at  $D = 0$ .

For the conduction band side ( $\nu_{\text{tot}} > 0$ ), three sets of LLs series, each starting from  $\nu_{\text{LL}} = +4$ , appear at  $\nu_{\text{tot}} \sim 2$ ,  $\sim 3.3$ , and 4, respectively. The  $\nu_{\text{LL}} = +4$  LL, clearly observed in the Hall resistance map of Fig. 2b, arises from the quantization of two Dirac bands in an interaction-induced topological trivial flat band gap. Besides, the observation of two series of LLs, with indexes of +12, +20, and +28 emanating from  $\nu_{\text{tot}} = 3$  and 3.3, is consistent with the doubling of the LLs index in a single Dirac band of +6, +10, +14. At  $\nu_{\text{tot}} > 4$ , a series of LLs with  $\nu_{\text{LL}} = +4, +12, +20, +28, +36$  suggest the exclusive contribution from Dirac bands to LLs spectrum. The observation of LLs at nonzero filling factors suggests interaction-induced energy gaps at integer fillings 2 and 3, as well as the fractional filling

10/3 of the flat band. We infer that the ground state at fractional filling 10/3 is a charge density wave state, analogous to that observed in alternating twisted trilayer graphene<sup>30,36</sup>.

For the valence band side ( $\nu_{\text{tot}} < 0$ ), by contrast, an irregular LL series is observed, despite the continuum model calculation predicting symmetric band structures for both sides. The first LL index from  $\nu_{\text{tot}} = -2$  is  $\nu_{LL} = -6$ , instead of -4; additionally, the LLs from  $\nu_{\text{tot}} = -4$ , with  $\nu_{LL} = -5, -14$ , and -24, deviate from the expected order in the two Dirac bands picture. The former could be attributed to a topological nontrivial energy gap with  $C = -2$  at  $\nu_{\text{flat}} = -2$ , while the latter contradicts predictions from the continuum model. This anomaly suggests hybridization between the flat and Dirac bands at  $D = 0$ . Note that the lattice reconstruction in a small twist angle device could induce an asymmetry between the conduction and valence bands<sup>35</sup>.

We can quantitatively extract the chemical potential and carrier density of Dirac bands<sup>7,30</sup> according to the trajectory of  $R_{xx}$  maximum which corresponds to the  $N$ th LL of Dirac bands. At these maximum points, the chemical potential difference between the  $N$ th LL ( $N_{LL} > 0$  for conduction band) and zeroth LL is expressed as  $\mu_N - \mu_0 = v_F \sqrt{2e\hbar N_{LL} B}$ , where  $v_F$  is the Fermi velocity of Dirac bands and  $\hbar$  is reduced Planck constant. In the continuum model,  $v_F$  is renormalized to  $\sim 6.1 \times 10^5$  m/s. The carrier density of Dirac bands is expressed as  $n_{\text{Dirac}} = 2N_{LL} \times 4eB/h$ . The chemical potential extracted from  $N_{LL} = 1$  and  $N_{LL} = 2$  trajectories, shown in Fig. 2d, provides an experimental estimation of the flat band bandwidth,  $\sim 50$  meV, significantly larger than  $\sim 10$  meV predicted by the continuum model. This large discrepancy suggests a nonrigid flat band, where strong electron-electron interactions lead to a band broadening effect by introducing many-body energy gaps<sup>37</sup>. In Fig. 2e, the carrier density contributed by Dirac bands is  $\sim 0.96 \times 10^{12}$  /cm<sup>2</sup> at  $\nu_{\text{tot}} = 4$ , one order larger than the simulation result, which directly arises from the band broadening effect.

In addition, both the chemical potential and carrier density show a plateau from  $\nu_{\text{tot}} \sim 1.64$  to  $\nu_{\text{tot}} \sim 2.36$ , suggesting the flat band is highly compressible at these doping. Afterward, they rapidly increase when  $\nu_{\text{tot}} > \sim 2.36$ , suggesting a correlated gap opens in the flat band and Dirac bands start to fill once again. Thus, we attribute the  $\nu_{\text{tot}} \sim 2.36$  as the onset of the gap opening or cascade transition of the flat band at half filling, i.e.  $\nu_{\text{flat}}$  is equal to 2 at  $\nu_{\text{tot}} \sim 2.36$ .

The abovementioned distinction between  $\nu_{\text{flat}}$  and  $\nu_{\text{tot}}$  is further confirmed in the Hall resistance measurement. As shown in Supplementary Fig. 3a, there are two regions where the Hall resistance reaches maximum marked by yellow dashed lines near  $\nu_{\text{tot}} = \pm 2$  at low displacement field. The maximized Hall resistance indicates that the Hall carrier density  $n_H = B/(e R_{xy})$  resets to almost zero, in agreement with the cascade transition of the flat band at half filling. As shown in the shaded regime in Supplementary Fig. 3b, the calculated  $\nu_{\text{tot}} - \nu_H$  clearly shows two symmetry breaking regions with  $\nu_{\text{tot}} - \nu_H \sim \pm 2$ , one starting from  $\nu_{\text{tot}} \sim 2.3$  and the other starting from  $\nu_{\text{tot}} \sim -2$ , further indicating the emergence of a symmetry breaking Fermi surface after the cascade transition at the half filling of flat band. We take the Hall carrier density as an approximation for the real carrier density in a minimal assumption. As shown in Fig. 2f,  $n_H$  almost equals to  $n_{\text{Dirac}}$  at  $\nu_{\text{tot}} \sim 2.3$  ( $\nu_{\text{flat}} \sim 1.96$ ). It suggests the free carrier density from the flat band is negligible around the half filling of flat band due to the emerging correlated energy gap. Beyond the full filling ( $\nu_{\text{tot}} > 4$ ), the Hall carrier density follows a linear relation

with the doping level,  $n_H = (\nu_{\text{tot}} - \nu_0) n_0/4$ , suggesting the carrier density is exclusively contributed by Dirac bands.

### C. Superconductivity and BCS to BEC Transitions at Zero Displacement Field

Next, we revisit the superconductivity with a quantitative analysis of the carrier density. Fig. 3a shows the superconducting phase diagram at  $D = 0$  V/nm, from which the critical temperature  $T_c$  is extracted and shown in Fig. 3b. Here we define  $T_c$  as the temperature at which  $R_{xx}$  reaches 40% of the normal state (details in Methods) accompanied by an error bar spanning from 30% to 50%. As shown in Fig. 3a and 3b, the superconductivity in the conduction band is well developed with higher  $T_c$  than that in the valance band. In the following, we focus on the conduction band side. The superconductivity, emerging at  $\nu_{\text{tot}} = 2$  and vanishing at  $\nu_{\text{tot}} = 4$ , shows a double dome-like shape with two local maximum  $T_c$  of  $\sim 1.2$  K at  $\nu_{\text{tot}} = 2.3$  and  $\nu_{\text{tot}} = 2.8$ . The observation of maximized  $T_c$  at  $\nu_{\text{tot}} = 2.3$  is unexpected. This is markedly distinct from the case of twisted bilayer graphene, where the superconductivity is strongly suppressed at half-filling due to the dominating correlated insulating state<sup>4</sup>. The overwhelming superconducting behavior at  $\nu_{\text{flat}} = 2$  suggests a collaboration instead of competition between the superconducting ground state and the high temperature correlated state.

To quantitatively estimate the coupling strength of Cooper pairs in the superconducting phase, we compare the superconducting coherence length and inter-particle distance  $d$ . The Ginzburg – Landau (G-L) coherence length  $\zeta$  is extracted from the critical magnetic field, i.e.  $\zeta = \sqrt{\Phi_0/(2\pi B_{c0})}$ , where  $\Phi_0 = h/(2e)$  is the superconducting flux quantum and  $B_{c0}$  is the critical magnetic field extrapolated to the zero-temperature limit. In Fig. 3b, the coherence length  $\zeta$  shows a non-monotonic dependence on  $\nu_{\text{tot}}$ , with a maximum value of  $\sim 100$  nm at  $\nu_{\text{tot}} = 2.5$  and a minimum of  $\sim 50$  nm at  $\nu_{\text{tot}} = 3.6$ . The inter-particle distance  $d$  can be approximated as inversely proportional to the Fermi vector  $k_F$ , i.e.  $1/d \sim k_F = \sqrt{4\pi n^*/g}$ , where  $n^*$  is the pairing carrier density and  $g = 2$  is the band degeneracy by considering the symmetry breaking at half filling. The way to define  $n^*$  or equivalently  $\nu^*$  can be expressed as  $\nu^* = |\nu_{\text{flat}} - 2|$ , where  $\nu^*$  is counted from the half filling of flat band. As shown in Fig. 3c, the product of  $\zeta$  and  $k_F$ , expressing the ratio between the coherence length and inter-particle distance, gives an evaluation of the coupling strength. The coupling strength becomes stronger when  $\nu_{\text{tot}}$  closes to 2.36 ( $\nu_{\text{flat}} = 2$ ), which is ascribed to the dilute pairing density at the half filling. The value of  $\zeta \times k_F$  is between 2  $\sim$  4 in dilute limit, approaching the onset of BEC ( $\sim 2.2$ ) in theoretical calculation<sup>38</sup>. By doping away from the half filling, it increases quickly and keeps the value above 10, close to the BCS limit. In this regard, the superconductivity at  $D = 0$  V/nm can be tuned from the BEC to the BCS limit by changing the doping level. Note that we overestimate the product since not all the carriers are paired in the superconducting regime. The superconductivity in AQTG could in principle be deep in the strong coupling regime.

### D. Electrical Field Tunable Coupling Strength of Superconductivity

To further modulate the coupling strength of the superconductivity, we apply a displacement field to introduce band hybridization and investigate the  $D$  dependence of coherent length and critical temperature. Fig. 4a exhibits the superconductivity phase diagram as a function of  $D$  at  $\nu_{\text{tot}} = 2.31$ . By

applying  $D$  from 0 to 0.25 V/nm, the superconductivity is enhanced with  $T_c$  increasing from 1.2 to 2 K; further increasing the  $D$ ,  $T_c$  decreases and eventually vanishes at  $D > \sim 0.4$  V/nm. The measured G-L coherence length  $\xi$  shows opposite  $D$  dependence, reaching a minimum  $\xi$  of  $\sim 30$  nm at  $D = 0.25$  V/nm (Fig. 4b). The resulted  $D$  dependent coupling strength from the product  $\xi \times k_F$  is shown in Fig 4c.  $\xi \times k_F$  is always kept below 6 and reaches 2 at  $D = 0.25$  V/nm, which suggests the superconductivity is modulated in a small regime around the BEC limit.

The strongly coupled superconductivity modulated by  $D$  is unconventional. In Fig. 4d,  $n_H$  is extracted at  $B_\perp = 0.5$  T when the superconductivity is fully suppressed. It keeps constant within  $|D| < 0.3$  V/nm and then rapidly diverges. The divergent  $n_H$  suggests a large DOS close to van Hove singularity (VHS), while  $T_c$  decreases and coupling strength weakens when  $|D| > 0.3$  V/nm. This observation is inconsistent with the conventional BCS prediction. In addition, the  $dV/dI$  curves in Fig. 4e show a higher critical current at finite  $D$  than that at zero  $D$ , suggesting a stronger coupling superconductivity closing to the limit of BEC regime. The insulating behavior of  $dV/dI$  (Fig. 4f) in the normal state above critical current deviates from the conventional metal behavior. The strong correlation between electrons potentially leads to a pseudo energy gap of pre-paired electrons.

### E. Critical currents and superfluid stiffness

We further quantify the superconductivity from the critical current measurements. Doping dependent  $dV/dI$  maps at  $D = 0.26$  V/nm show two boundaries with distinct critical currents (Fig. 5a-b). The lower boundary  $j_s$  vanishes with the increase of magnetic field while the higher boundary  $j_n$  remains evident. The rapid suppression upon magnetic field suggests the lower boundary corresponds to the critical current of superconductivity. While the higher boundary is ascribed to the critical behavior of a correlated gap at the half filling, resulting from interband transitions via the Zener-Klein tunnelling<sup>39-42</sup> at high current density. Importantly, we further estimate the Fermi velocity of the flatband from the drift velocity ( $v_n$ ) calculated from the higher critical current density, according to the formula  $v_n = \frac{1}{e} \frac{dj_n}{dn}$ . The calculated  $v_n \approx 1700$  m/s suggests an extremely flat dispersion, with the same order of magnitude as those in magic angle TBG<sup>41</sup>. With the drift velocity, superconducting quantities such as pairing gap can be estimated as  $\Delta \approx \hbar v_n / \xi$ . Using  $\xi = 30$  nm and  $T_c = 2$  K at  $D = 0.26$  V/nm, we obtain  $\Delta / k_B T_c \approx 0.2$ , one order lower than the BCS prediction of 1.75. In addition, we calculate the superfluid stiffness at zero temperature limit using the critical current density  $j_s$  in Fig. 5c, based on the formula of  $D_s = \frac{2\pi j_s \xi}{\Phi_0}$  in flat band condition<sup>41</sup>. As shown in Fig. 5d,  $D_s$  reaches the maximum of  $\sim 4 \times 10^7$  /H around  $D = 0.26$  V/nm, one order larger than the conventional contribution of  $D_s = \frac{e^2 n^*}{m^*}$  (the red dashed line in Fig. 5d), where effective mass is approximated as  $m^* = \hbar k_F / v_n$ . As  $D$  drives the system close to VHS,  $D_s$  rapidly decreases and approaches the level of conventional contribution.

The enhanced coupling strength and superfluid stiffness tuned by  $D$  can be attributed to the increasing contribution of quantum metric. In flat band superconductivity, quantum metric contributions are comparable to or even larger than conventional contributions<sup>43-45</sup>, and can be further amplified by the

band touching in multiband systems<sup>46</sup>. As shown in Supplementary Fig. 5, the ratio between onset temperature  $T^*$  and  $T_{\text{BKT}}$  increases from 1.45 to 2.19 with  $D$ , validating the strong coupling induced by quantum geometry<sup>47</sup> at large  $D$ . Notably, recent kinetic inductance measurements also reveal possible nodal superconductivity in ATMG<sup>48</sup> and indispensable contribution of quantum metric to superfluid stiffness in TBG<sup>49</sup>.

### III. CONCLUSIONS

In conclusion, we investigate unconventional superconductivity in a field-tunable multi-band system. Our study elucidates individual contributions from flat and dispersive bands. By exploring the doping- and  $D$ -tunable coupling strength of superconductivity, we observe a signature of the BCS to BEC crossover. Notably, the strong coupling superconductivity is observed near the half filling of flat band and can be further modulated by  $D$ . Moreover, we reveal the unconventional superconductivity with vanishing Fermi velocity and large superfluid stiffness, which goes beyond the conventional BCS prediction and could be ascribed to significant quantum metric driven by  $D$  when the Dirac bands touch flat band. Our findings pave the way for a better understanding of unconventional superconductivity and BCS-BEC crossover in multiband systems.

### Acknowledgments

We thank Fengcheng Wu, Zhida Song, Kun Jiang, Shiliang Li, and Kui Jin for useful discussions. We acknowledge support from the National Key Research and Development Program (Grant No. 2020YFA0309600), the Natural Science Foundation of China (NSFC, Grant Nos. 12074413, 61888102, 11834017,), the Strategic Priority Research Program of CAS (Grant No. XDB33000000) and the Key-Area Research and Development Program of Guangdong Province (Grant No. 2020B0101340001). K.W. and T.T. acknowledge support from the Elemental Strategy Initiative conducted by the MEXT, Japan (Grant No. JPMXP0112101001), JSPS KAKENHI (Grant Nos. 19H05790, 20H00354 and 21H05233) and A3 Foresight by JSPS.

### Author contributions

W.Y. and G.Z. supervised the project. W.Y. and L.L. designed the experiments. L.L. fabricated the devices. L.L. and Y.H. performed the magneto-transport measurement. L.L. performed the calculations. K.W. and T.T. provided hexagonal boron nitride crystals. L.L., C.Z., K.L., G.Z., and W.Y. analyzed the data. L.L. and W.Y. wrote the paper with the input from all the authors.

### Data availability

The data that support the findings of this study are available from the corresponding authors upon reasonable request.

### Competing interests

The authors declare no competing interests.

## Additional information

Supplementary information is provided online

## Reference

1. Zhou, X. *et al.* High-temperature superconductivity. *Nat Rev Phys* **3**, 462–465 (2021).
2. Molodyk, A. & Larbalestier, D. C. The prospects of high-temperature superconductors. *Science* **380**, 1220–1222 (2023).
3. Bistritzer, R. & MacDonald, A. H. Moiré bands in twisted double-layer graphene. *Proc. Natl. Acad. Sci. U.S.A.* **108**, 12233–12237 (2011).
4. Cao, Y. *et al.* Unconventional superconductivity in magic-angle graphene superlattices. *Nature* **556**, 43–50 (2018).
5. Lu, X. *et al.* Superconductors, orbital magnets and correlated states in magic-angle bilayer graphene. *Nature* **574**, 653–657 (2019).
6. Yankowitz, M. *et al.* Tuning superconductivity in twisted bilayer graphene. *Science* **363**, 1059–1064 (2019).
7. Park, J. M., Cao, Y., Watanabe, K., Taniguchi, T. & Jarillo-Herrero, P. Tunable strongly coupled superconductivity in magic-angle twisted trilayer graphene. *Nature* **590**, 249–255 (2021).
8. Hao, Z. *et al.* Electric field-tunable superconductivity in alternating-twist magic-angle trilayer graphene. *Science* **371**, 1133–1138 (2021).
9. Oh, M. *et al.* Evidence for unconventional superconductivity in twisted bilayer graphene. *Nature* **600**, 240–245 (2021).
10. Park, J. M. *et al.* Robust superconductivity in magic-angle multilayer graphene family. *Nat. Mater.* **21**, 877–883 (2022).
11. Zhang, Y. *et al.* Promotion of superconductivity in magic-angle graphene multilayers. *Science* **377**, 1538–1543 (2022).
12. Kim, H. *et al.* Evidence for unconventional superconductivity in twisted trilayer graphene. *Nature* **606**, 494–500 (2022).
13. Cao, Y. *et al.* Correlated insulator behaviour at half-filling in magic-angle graphene superlattices. *Nature* **556**, 80–84 (2018).
14. Cao, Y. *et al.* Tunable correlated states and spin-polarized phases in twisted bilayer–bilayer graphene. *Nature* **583**, 215–220 (2020).
15. Liu, X. *et al.* Tunable spin-polarized correlated states in twisted double bilayer graphene. *Nature* **583**, 221–225 (2020).
16. Shen, C. *et al.* Correlated states in twisted double bilayer graphene. *Nat. Phys.* **16**, 520–525 (2020).
17. Liu, L. *et al.* Isospin competitions and valley polarized correlated insulators in twisted double bilayer graphene. *Nat Commun* **13**, 3292 (2022).
18. Chen, S. *et al.* Electrically tunable correlated and topological states in twisted monolayer-bilayer graphene. *Nat. Phys.* **17**, 374–380 (2021).



19. Chen, G. *et al.* Evidence of a gate-tunable Mott insulator in a trilayer graphene moiré superlattice. *Nat. Phys.* **15**, 237–241 (2019).
20. Sharpe, A. L. *et al.* Emergent ferromagnetism near three-quarters filling in twisted bilayer graphene. *Science* **365**, 605–608 (2019).
21. Chen, G. *et al.* Tunable correlated Chern insulator and ferromagnetism in a moiré superlattice. *Nature* **579**, 56–61 (2020).
22. Liu, L. *et al.* Observation of First-Order Quantum Phase Transitions and Ferromagnetism in Twisted Double Bilayer Graphene. *Phys. Rev. X* **13**, 031015 (2023).
23. Park, H. *et al.* Observation of fractionally quantized anomalous Hall effect. *Nature* **622**, 74–79 (2023).
24. Xu, F. *et al.* Observation of Integer and Fractional Quantum Anomalous Hall Effects in Twisted Bilayer MoTe<sub>2</sub>. *Phys. Rev. X* **13**, 031037 (2023).
25. Lu, Z. *et al.* Fractional quantum anomalous Hall effect in multilayer graphene. *Nature* **626**, 759–764 (2024).
26. Serlin, M. *et al.* Intrinsic quantized anomalous Hall effect in a moiré heterostructure. *Science* **367**, 900–903 (2020).
27. Polshyn, H. *et al.* Electrical switching of magnetic order in an orbital Chern insulator. *Nature* **588**, 66–70 (2020).
28. Li, T. *et al.* Quantum anomalous Hall effect from intertwined moiré bands. *Nature* **600**, 641–646 (2021).
29. Song, Z.-D. & Bernevig, B. A. Magic-Angle Twisted Bilayer Graphene as a Topological Heavy Fermion Problem. *Phys. Rev. Lett.* **129**, 047601 (2022).
30. Shen, C. *et al.* Dirac spectroscopy of strongly correlated phases in twisted trilayer graphene. *Nat. Mater.* **22**, 316–321 (2023).
31. Burg, G. W. *et al.* Emergence of correlations in alternating twist quadrilayer graphene. *Nat. Mater.* **21**, 884–889 (2022).
32. Khalaf, E., Kruchkov, A. J., Tarnopolsky, G. & Vishwanath, A. Magic angle hierarchy in twisted graphene multilayers. *Phys. Rev. B* **100**, 085109 (2019).
33. Cao, Y., Park, J. M., Watanabe, K., Taniguchi, T. & Jarillo-Herrero, P. Pauli-limit violation and re-entrant superconductivity in moiré graphene. *Nature* **595**, 526–531 (2021).
34. Kim, K. *et al.* van der Waals Heterostructures with High Accuracy Rotational Alignment. *Nano Lett.* **16**, 1989–1995 (2016).
35. Carr, S. *et al.* Ultraheavy and Ultrarelativistic Dirac Quasiparticles in Sandwiched Graphenes. *Nano Lett.* **20**, 3030–3038 (2020).
36. Siriviboon, P. *et al.* A new flavor of correlation and superconductivity in small twist-angle trilayer graphene. Preprint at <http://arxiv.org/abs/2112.07127> (2022).
37. Xie, Y. *et al.* Spectroscopic signatures of many-body correlations in magic-angle twisted bilayer graphene. *Nature* **572**, 101–105 (2019).
38. Chen, Q., Wang, Z., Boyack, R., Yang, S. & Levin, K. When superconductivity crosses over: From BCS to BEC. *Rev. Mod. Phys.* **96**, 025002 (2024).
39. Yang, W. *et al.* A graphene Zener–Klein transistor cooled by a hyperbolic substrate. *Nature Nanotech* **13**, 47–52 (2018).

40. Berdyugin, A. I. *et al.* Out-of-equilibrium criticalities in graphene superlattices. *Science* **375**, 430–433 (2022).
41. Tian, H. *et al.* Evidence for Dirac flat band superconductivity enabled by quantum geometry. *Nature* **614**, 440–444 (2023).
42. Schmitt, A. *et al.* Mesoscopic Klein-Schwinger effect in graphene. *Nat. Phys.* **19**, 830–835 (2023).
43. Hu, X., Hyart, T., Pikulin, D. I. & Rossi, E. Geometric and Conventional Contribution to the Superfluid Weight in Twisted Bilayer Graphene. *Phys. Rev. Lett.* **123**, 237002 (2019).
44. Xie, F., Song, Z., Lian, B. & Bernevig, B. A. Topology-Bounded Superfluid Weight in Twisted Bilayer Graphene. *Phys. Rev. Lett.* **124**, 167002 (2020).
45. Chen, S. A. & Law, K. T. Ginzburg-Landau Theory of Flat-Band Superconductors with Quantum Metric. *Phys. Rev. Lett.* **132**, 026002 (2024).
46. Huhtinen, K.-E., Herzog-Arbeitman, J., Chew, A., Bernevig, B. A. & Törmä, P. Revisiting flat band superconductivity: Dependence on minimal quantum metric and band touchings. *Phys. Rev. B* **106**, 014518 (2022).
47. Wang, Z., Chaudhary, G., Chen, Q. & Levin, K. Quantum geometric contributions to the BKT transition: Beyond mean field theory. *Phys. Rev. B* **102**, 184504 (2020).
48. Banerjee, A. *et al.* Superfluid stiffness of twisted multilayer graphene superconductors. Preprint at <http://arxiv.org/abs/2406.13742> (2024).
49. Tanaka, M. *et al.* Kinetic Inductance, Quantum Geometry, and Superconductivity in Magic-Angle Twisted Bilayer Graphene. Preprint at <http://arxiv.org/abs/2406.13740> (2024).
50. Wang, L. *et al.* One-Dimensional Electrical Contact to a Two-Dimensional Material. *Science* **342**, 614–617 (2013).

## Figure & Figure captions

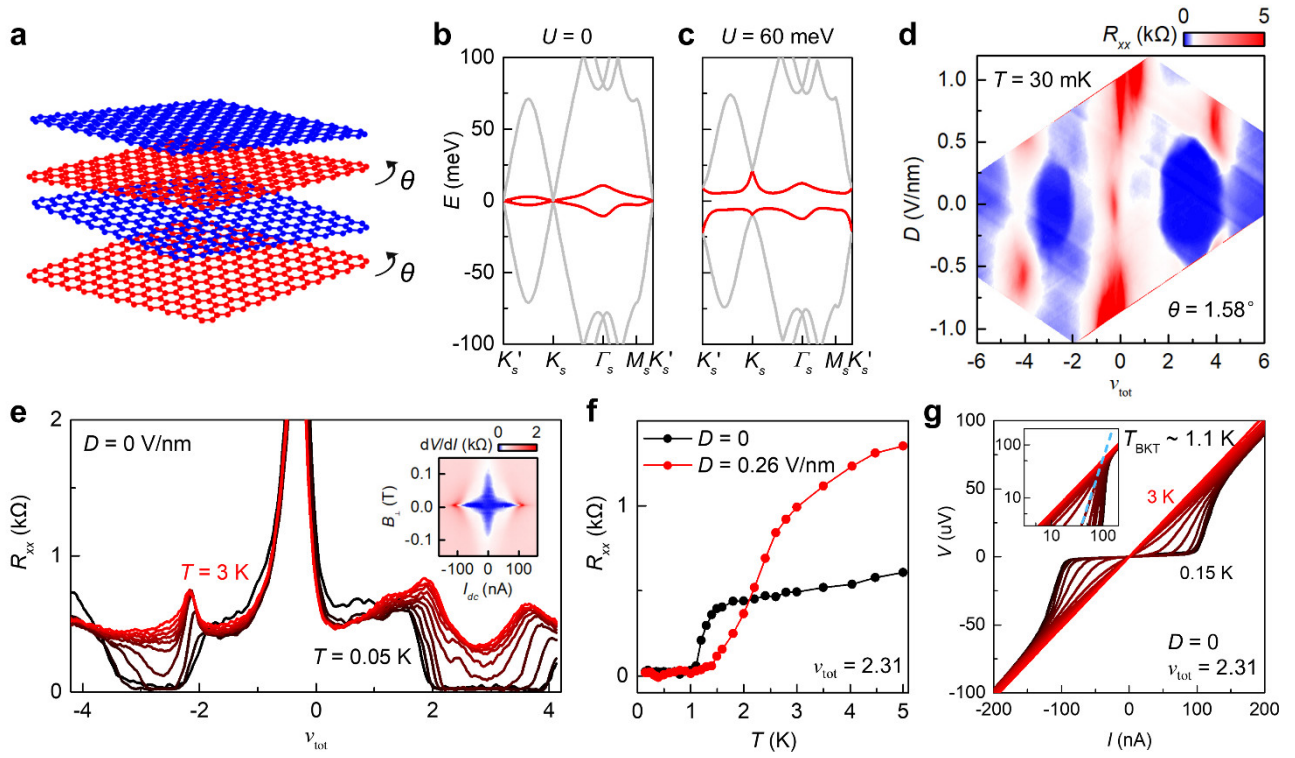


FIG. 1. Superconductivity in alternating twisted quadralayer graphene. **a**, Schematics of the stacking order of ATQG. **b**, **c**, Band structures calculated from the continuum model at  $U = 0$  and  $U = 60$  meV. **d**,  $R_{xx}$  as a function of  $\nu_{\text{tot}}$  and  $D$  at  $T = 30$  mK and  $B = 0$  T. **e**,  $R_{xx}$  versus  $\nu_{\text{tot}}$  from  $T = 0.05$  K to 3 K at  $D = 0$ . Inset,  $dV/dI$  as a function of  $I_{\text{dc}}$  and  $B$  at  $\nu_{\text{tot}} = 2.31$  and  $D = 0$ . **f**,  $R_{xx}$  versus  $T$  at  $D = 0$  and 0.26 V/nm. **g**,  $V$  versus  $I$  from  $T = 0.15$  K to 3 K. Inset, zoom-in figure in log-log coordinate. The blue dash line is the nonlinear fitting of  $V \sim I^3$ .

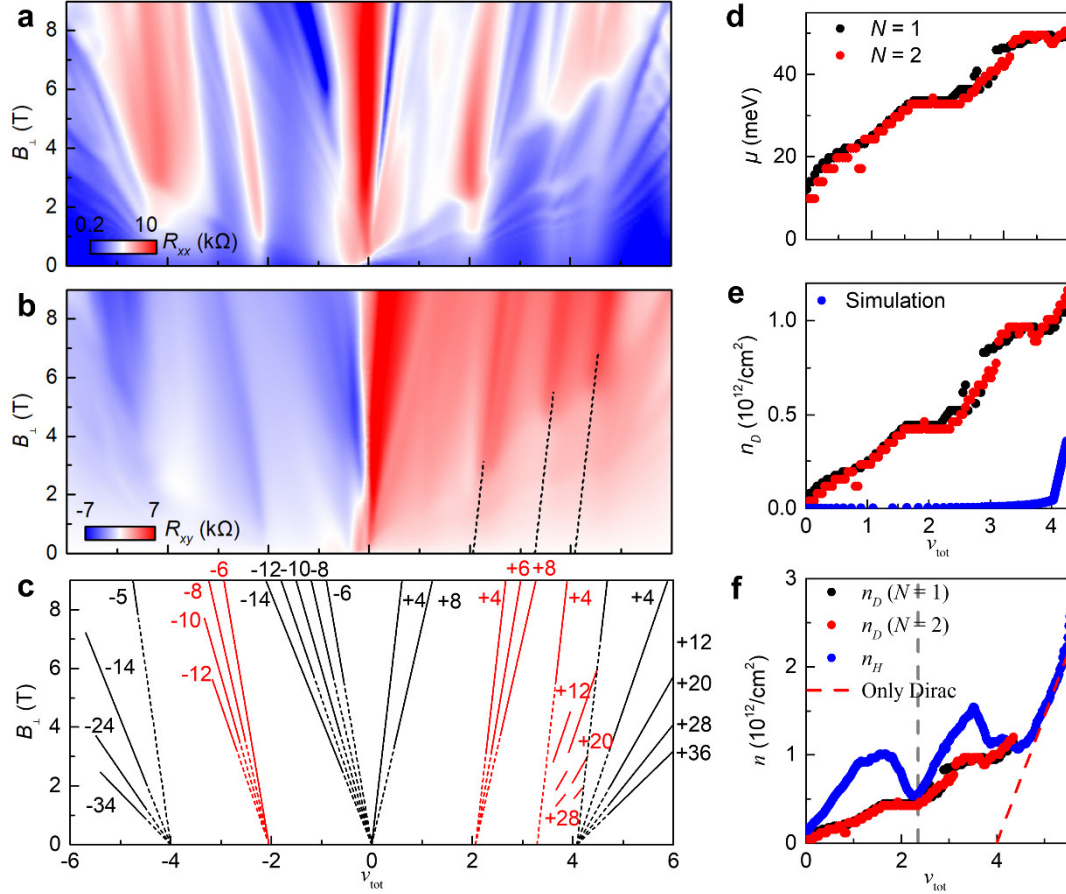


FIG. 2. Coexistence of flat and Dirac bands. **a-c**, Landau fan diagrams at  $D = 0$  and  $T = 1.7$  K. **d**,  $\mu$  versus  $\nu_{\text{tot}}$  of  $N = 1$  and 2 LL from the Dirac band. **e**,  $n_{\text{Dirac}}$  versus  $\nu_{\text{tot}}$  of  $N = 1$  and 2 LL from the Dirac band. The blue dot line is simulated carrier densities of Dirac bands. **f**, Carrier densities versus  $\nu_{\text{tot}}$ . The gray dashed line corresponds to  $\nu_{\text{flat}} = 2$ . The red dashed line corresponds to the fitting curve of  $n = (\nu_{\text{tot}} - \nu_0) n_0/4$ .

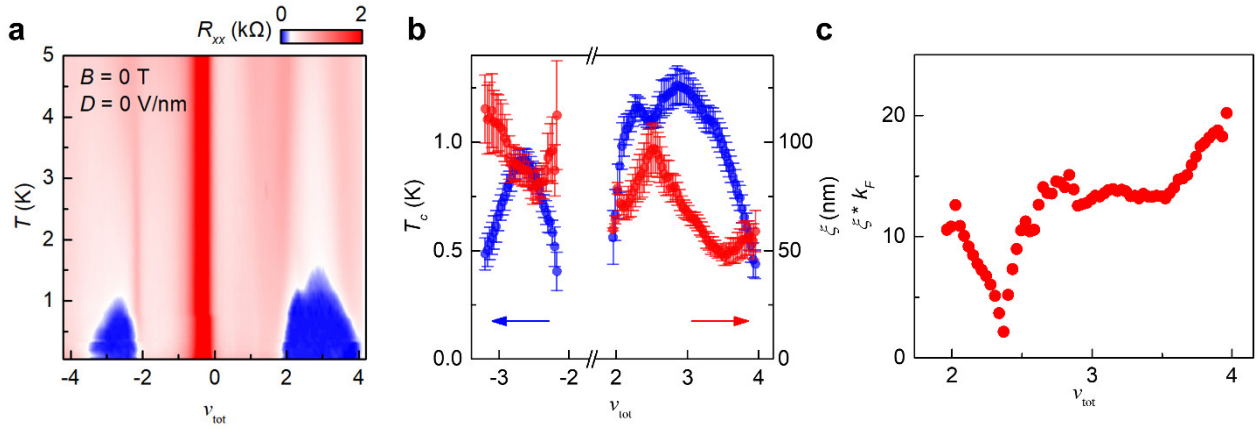


FIG. 3. Doping tunable superconductivity at  $D = 0$ . **a**,  $R_{xx}$  as a function of  $\nu_{tot}$  and  $T$ . **b**,  $T_c$  and  $\xi$  versus  $\nu_{tot}$ . **c**,  $\xi \times k_F$  versus  $\nu_{tot}$ .

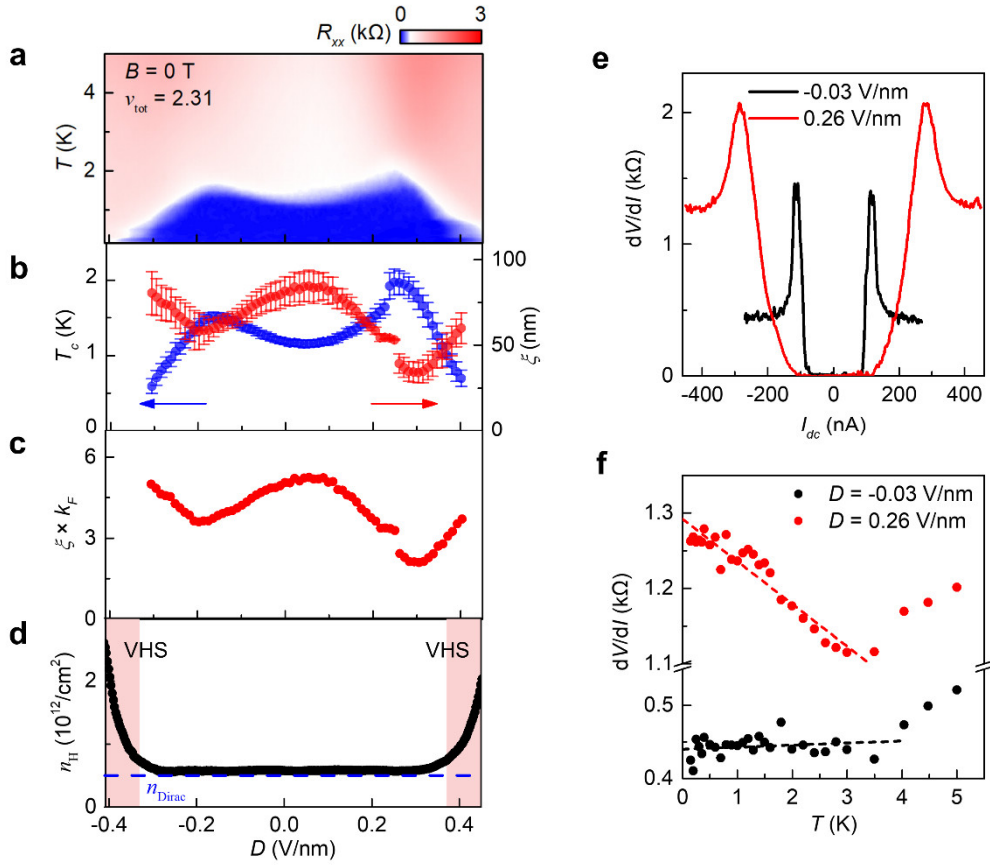


FIG. 4.  $D$  tunable coupling strength of superconductivity. **a**,  $R_{xx}$  as a function of  $D$  and  $T$  at  $\nu_{\text{tot}} = 2.31$ . **b**,  $T_c$  and  $\xi$  versus  $D$ . **c**,  $\xi \times k_F$  versus  $D$ . **d**,  $n_H$  versus  $D$ . The blue dashed line corresponds to the carrier density of Dirac bands. The pink regions are in the vicinity of VHS. **e**,  $dV/dI$  versus  $I_{\text{dc}}$  at different  $D$ . **f**,  $dV/dI$  versus  $T$ . The data is measured at  $I_{\text{dc}} = 265$  (420) nA and  $D = -0.03$  (0.26) V/nm.

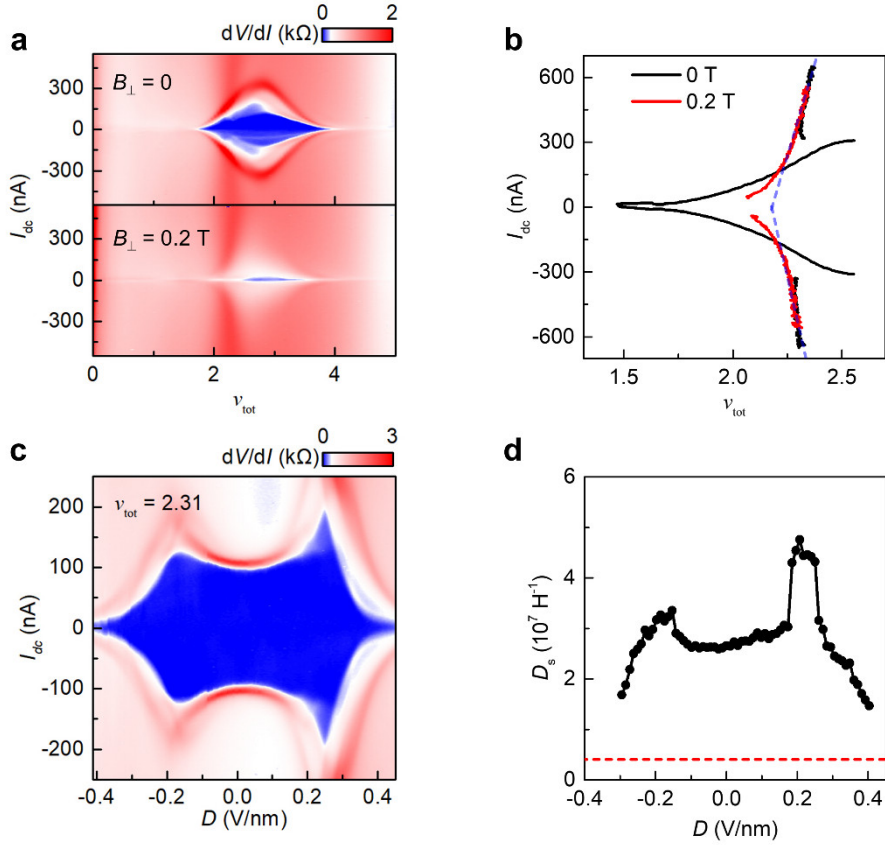


FIG. 5. Critical currents and superfluid stiffness. **a**,  $dV/dI$  as a function of  $\nu_{\text{tot}}$  and  $I_{\text{dc}}$  at  $D = 0.26$  V/nm. Top,  $B = 0$  T. Bottom,  $B_{\perp} = 0.2$  T. **b**, Extracted critical currents for superconductivity and correlated insulator. Blue dashed lines are linear fitting curves. **c**,  $dV/dI$  as a function of  $D$  and  $I_{\text{dc}}$  at  $\nu_{\text{tot}} = 2.31$ . **d**, calculated superfluid stiffness versus  $D$ . The red dashed line corresponds to conventional contribution without considering quantum metric.

**Supplementary Materials for**  
**“Probing electric field tunable multiband superconductivity in alternating twisted quadralayer graphene”**

Le Liu<sup>1,2</sup>, Yu Hong<sup>1,2</sup>, Chengping Zhang<sup>3</sup>, Jundong Zhu<sup>1,2</sup>, Jingwei Dong<sup>1,2</sup>, Kenji Watanabe<sup>4</sup>, Takashi Taniguchi<sup>5</sup>, LuoJun Du<sup>1,2</sup>, Dongxia Shi<sup>1,2,6</sup>, Kam Tuen Law<sup>3</sup>, Wei Yang<sup>1,2,6\*</sup>, Guangyu Zhang<sup>1,2,6\*</sup>

<sup>1</sup> *Beijing National Laboratory for Condensed Matter Physics and Institute of Physics, Chinese Academy of Sciences, Beijing 100190, China*

<sup>2</sup> *School of Physical Sciences, University of Chinese Academy of Sciences, Beijing, 100190, China*

<sup>3</sup> *Department of Physics, Hong Kong University of Science and Technology, Clear Water Bay, Hong Kong, China*

<sup>4</sup> *Research Center for Electronic and Optical Materials, National Institute for Materials Science, 1-1 Namiki, Tsukuba 305-0044, Japan*

<sup>5</sup> *Research Center for Materials Nanoarchitectonics, National Institute for Materials Science, 1-1 Namiki, Tsukuba 305-0044, Japan*

<sup>6</sup> *Songshan Lake Materials Laboratory, Dongguan 523808, China*

\* Corresponding authors. Email: [wei.yang@iphy.ac.cn](mailto:wei.yang@iphy.ac.cn); [gyzhang@iphy.ac.cn](mailto:gyzhang@iphy.ac.cn)



## Supplementary Note 1: Methods

**1.1. Device fabrication.** The alternating twisted quatralayer graphene (ATQG) sample is fabricated into the dual gate Hall bar device with a Ti/Au top gate and a graphite bottom gate. The device is 1D contacted with Cr/Au 3/30 nm after etching with a CHF<sub>3</sub>/O<sub>2</sub> mixture<sup>50</sup>.

**1.2. Device characterization.** Two gates configuration allows us to independently tune the carrier density  $n$  and the displacement field  $D$  as  $n = (C_b V_b + C_t V_t)/e$  and  $D = (C_b V_b - C_t V_t)/2\epsilon_0$ , where  $C_b$  ( $C_t$ ) is the geometrical capacitance per area for bottom (top) gate,  $V_b$  ( $V_t$ ) is the voltage applied on the bottom (top) gate,  $e$  is the electron charge, and  $\epsilon_0$  is the vacuum permittivity.

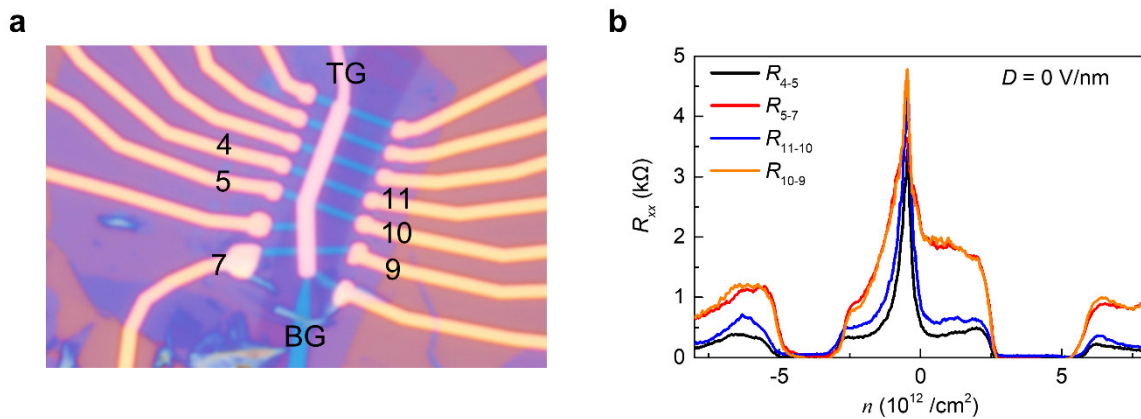
The cryogenic magneto-transport measurements are mainly carried out in Leiden dilution refrigerator CF-CS81 with a magnet of 14 T and an attocube sample stage with vertical and horizontal rotation axis, and a helium-4 bath cryostat with a magnet of 9 T. We measure the four terminal longitudinal resistance  $R_{xx}$  and Hall resistance  $R_{xy}$  using the lock-in amplifier LI5650 with a frequency of 7~20 Hz. Excitation currents are between  $I = 1\sim 10$  nA with a large series resistance 100 M $\Omega$ . The  $dV/dI$  measurements are carried out with a superposition of an AC signal ( $\sim 2$  nA) and a DC signal (maximum  $\sim 650$  nA).

**1.3. LLs spectrums in multiband system.** The Landau fan diagram of the multiband system can be understood from the following two aspects. Firstly, the total LL filling factor (Chern number) is the sum of that from dispersive bands and the flat band, i.e.  $\nu_{LL} = \nu_{LL-Dirac} + \nu_{LL-flat}$ . Secondly, the large density of states (DOS) of LLs of Dirac bands lead to a maximum in  $R_{xx}$  when the chemical potential within a compressible flat band is aligned with these LLs.

**1.4. Continuum model calculations.** We use the continuum model<sup>32</sup> to calculate the band structure. The parameters in continuum model are as following according to the references<sup>10,11,31</sup>:  $v_F = 0.9 \times 10^6$  m/s, AA site hopping energy  $w_{AA} = 64$  meV, AB site hopping energy  $w_{AB} = 106$  meV. Twisted angle is set as  $1.58^\circ$  which is slightly away from the magic angle of ATQG,  $\sim 1.75^\circ$ . Hence, the bandwidth of flat band is larger than that in the optimal case.

## Supplementary Note 2: The device homogeneity.

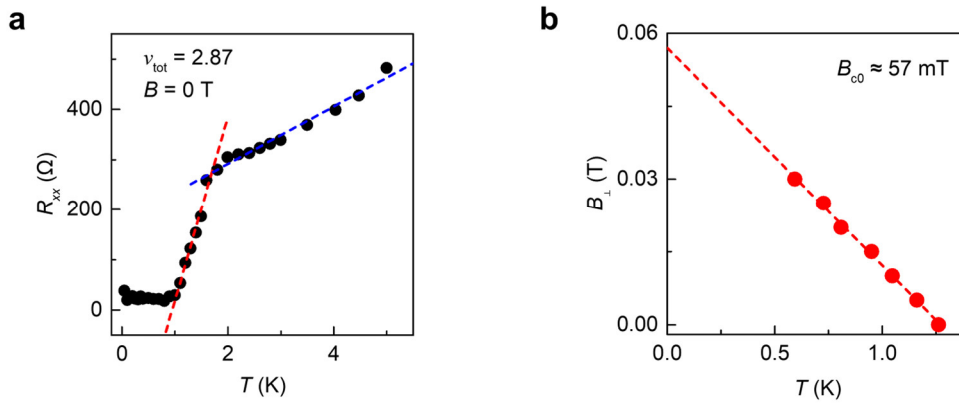
Supplementary Fig.1a shows the optical micrograph of the device with a twisted angle of  $1.58^\circ$ . The transport curves between different bars in Supplementary Fig.1b suggest the uniform angle distribution and the robust superconductivity in this device.



**Supplementary Fig. 1. The homogeneity of ATQG Device. a**, The optical micrograph of the ATQG device. **b**, Transport curves between different bars.

### Supplementary Note 3: The definition of $T_c$ and $B_{c0}$ .

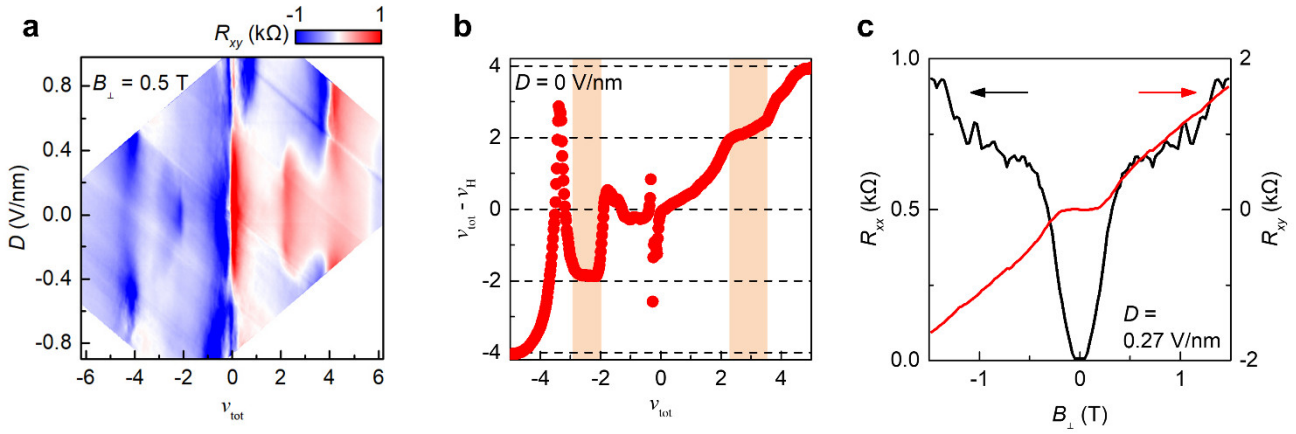
As shown in Supplementary Fig. 2a, the temperature dependent curve can be divided into three parts, zero resistance region, linear transition region, and high temperature metal region. Here the linear transition region and high temperature metal region can be linearly fitted by the curve of  $R = A_1 * T + B_1$  (red dashed line) and  $R = A_2 * T + B_2$  (blue dashed line). Then we define  $T_c$  as the temperature where  $R$  is at 40% of the intersection point  $R^*$  of two curves, and the error bar is defined as 30% ~ 50% of  $R^*$ .  $B_{c0}$  is extracted by linearly extrapolating the fitting curve  $B_c$  versus  $T$  to zero temperature limit (Supplementary Fig. 2b).



**Supplementary Fig. 2.  $T_c$  and critical magnetic field. a**,  $T_c$  is defined by the intersection point of two linear fitting lines. **b**, The critical magnetic field at zero temperature extracted by linear fitting.

### Supplementary Note 4: Cascade transitions.

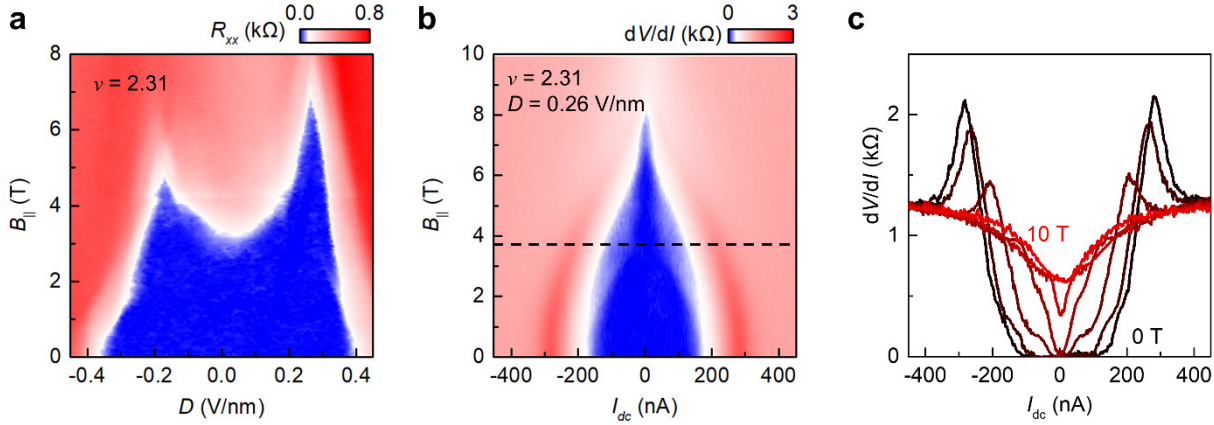
As shown in Supplementary Fig. 3a, the Hall resistance exhibits a signature of cascade transitions around  $\nu_{\text{tot}} = \pm 2$ , where the carrier density is reset to zero due to the flavor polarization (Supplementary Fig. 3b). In Supplementary Fig. 3c, the Hall resistance is zero in the superconducting phase and gradually evolves to a linear dependence on  $B$ . We extract the Hall carrier density in this linear region.



**Supplementary Fig. 3. Cascade transitions at half filling.** **a**,  $R_{xy}$  as a function of  $\nu_{\text{tot}}$  and  $D$  at  $B_{\perp} = 0.5$  T. The yellow dashed lines correspond to the cascade transition at half filling of the flat band. **b**,  $\nu_{\text{tot}} - \nu_H$  versus  $\nu_{\text{tot}}$  at  $D = 0$ . **c**,  $R_{xx}$  and  $R_{xy}$  versus  $B_{\perp}$  at  $D = 0.27$  V/nm.

### Supplementary Note 5: The superconductivity beyond the Pauli limit.

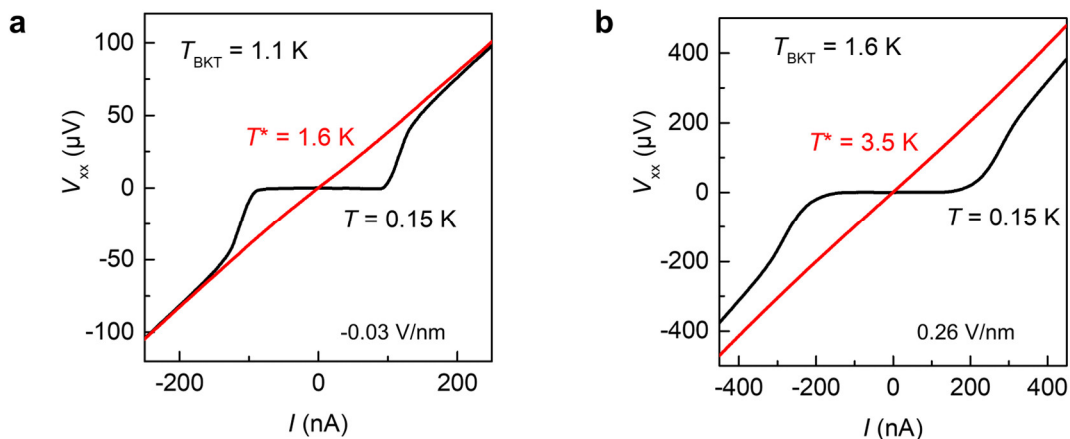
As shown in Supplementary Fig. 4, the superconductivity can survive in a parallel magnetic field as high as 7 T at  $D \sim 0.26$  V/nm. This critical field is nearly twice of the Pauli limit, which is defined as  $B_p = 1.86 \text{ T/K} \times T_c$  in the conventional superconductivity. Here,  $B_p \sim 3.7$  T at  $D = 0.26$  V/nm, half the critical field of  $\sim 7$  T.



**Supplementary Fig. 4. Parallel magnetic field responses.** **a**,  $R_{xx}$  as a function of  $D$  and  $B_{||}$  at  $\nu_{\text{tot}} = 2.31$ . **b**,  $dV/dI$  as a function of  $I_{dc}$  and  $B_{||}$  at  $\nu_{\text{tot}} = 2.31$  and  $D = 0.26$  V/nm. The black dashed line corresponds to the Pauli limit of  $B_p = 1.86 \text{ T/K} \times T_c$ . **c**,  $dV/dI$  versus  $I_{dc}$  from  $B_{||} = 0$  to 10 T.

### Supplementary Note 6: Pairing and condensation.

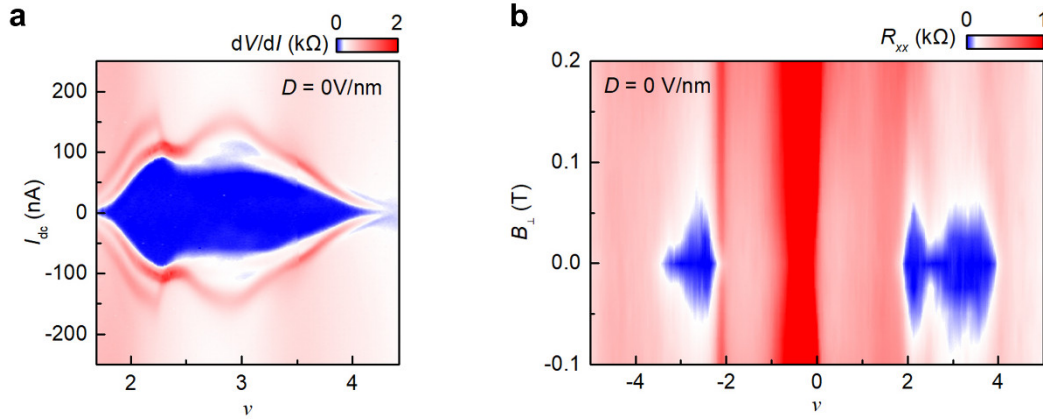
The pairing onset temperature  $T^*$  is defined as the onset of non-linear  $I$ - $V$  curves. The ratio between  $T^*$  and  $T_{\text{BKT}}$  is different between  $D = 0$  and  $D = 0.26$  V/nm. The higher value (2.19) at  $D = 0.26$  V/nm suggests a stronger coupling superconducting behavior.



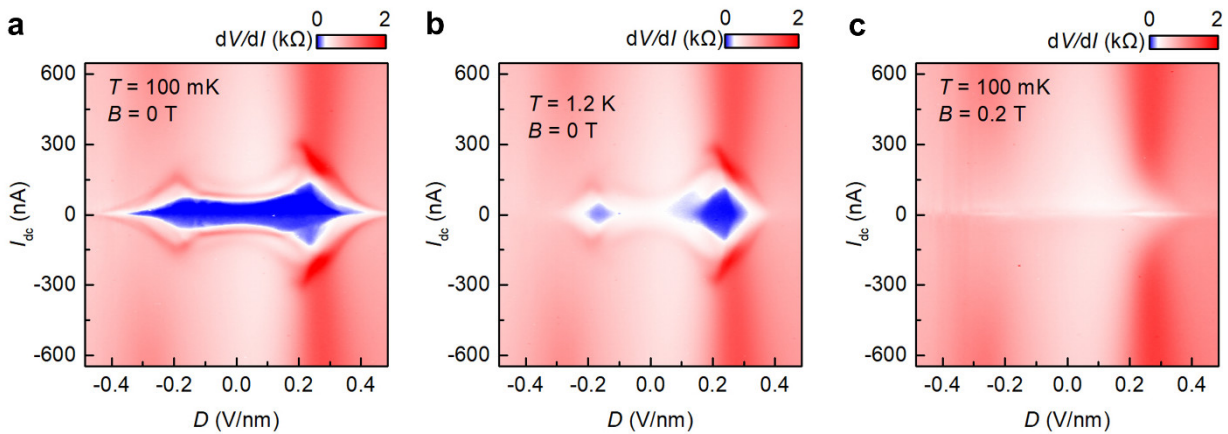
Supplementary Fig. 5. Pairing onset temperature. a, b,  $V_{xx}$  versus  $I$  at  $D = -0.03$  and  $0.26$  V/nm.

**Supplementary Note 6: The response of superconductivity to external fields.**

Here, Supplementary Fig. 6 and 7 show more data about the response of superconductivity under the current excitation and magnetic field.



**Supplementary Fig. 6. Superconductivity at  $D = 0$ .** **a**,  $dV/dI$  as a function of  $\nu$  and  $I_{dc}$ . **b**,  $R_{xx}$  as a function of  $\nu$  and  $B_{\perp}$ .



**Supplementary Fig. 7. Superconductivity at  $\nu = 2.31$ .** **a-c**,  $dV/dI$  as a function of  $D$  and  $I_{dc}$  at  $\nu = 2.31$ .